



Riming in winter  
alpine snowfall  
during CLACE 2014

J. Grazioli et al.

# Riming in winter alpine snowfall during CLACE 2014: polarimetric radar and in-situ observations

J. Grazioli<sup>1</sup>, G. Lloyd<sup>2</sup>, L. Panziera<sup>1</sup>, P. J. Connolly<sup>2</sup>, J. Henneberger<sup>3</sup>, and A. Berne<sup>1</sup>

<sup>1</sup>Environmental Remote Sensing Laboratory (LTE), École Polytechnique Fédérale de Lausanne (EPFL), Lausanne, Switzerland

<sup>2</sup>Centre for Atmospheric Science, University of Manchester, Manchester, UK

<sup>3</sup>Institute for Atmospheric and Climate Science, ETH, Zurich, Switzerland

Received: 05 June 2015 – Accepted: 11 June 2015 – Published: 02 July 2015

Correspondence to: A. Berne (alexis.berne@epfl.ch)

Published by Copernicus Publications on behalf of the European Geosciences Union.

Title Page

Abstract

Introduction

Conclusions

References

Tables

Figures



Back

Close

Full Screen / Esc

Printer-friendly Version

Interactive Discussion



## Abstract

This study investigates the microphysics of winter alpine snowfall occurring in mixed-phase clouds in an inner-Alpine valley during January and February 2014. The available observations include high resolution polarimetric radar and in-situ measurements of the ice-phase and liquid-phase components of clouds and precipitation. Radar-based hydrometeor classification suggests that riming is a dominant factor leading to an efficient growth of the precipitating mass and to a large snow accumulation on the ground. The time steps during which rimed precipitation is dominant are analysed in terms of temporal evolution and vertical structure. In most cases, riming is the result of a turbulent phase, of limited duration, during which supercooled liquid water (SLW) is available. When this turbulent layer is stable in time and continuously provides SLW, riming can be sustained for many hours without SLW depletion, thus generating large accumulations of snow. The microphysical interpretation as well as the meteorological situation associated with one event with those characteristics are detailed in the manuscript. The vertical structure of polarimetric radar observations during intense rimed precipitation shows a peculiar maximum of specific differential phase shift  $K_{dp}$ , associated with large number concentrations and/or heavy riming of anisotropic crystals. Below this  $K_{dp}$  peak there is usually an enhancement in  $Z_H$ , proportional to the  $K_{dp}$  enhancement and interpreted as aggregation of ice crystals.

## 1 Introduction

Precipitation of ice-phase hydrometeors is the result of the interactions between cloud ice crystals, supercooled liquid water (SLW) droplets and water vapour. After nucleation, the processes of vapour deposition, aggregation, and riming all contribute to the growth of the crystals up to the point where they begin to fall and further interact with the lower layers of the atmosphere (e.g., Pruppacher and Klett, 1997; Cantrell and Heymsfield, 2005; Straka and Mansell, 2005). The characteristics of the ice-phase hy-

ACPD

15, 18065–18108, 2015

## Riming in winter alpine snowfall during CLACE 2014

J. Grazioli et al.

Title Page

Abstract

Introduction

Conclusions

References

Tables

Figures



Back

Close

Full Screen / Esc

Printer-friendly Version

Interactive Discussion



drometeors at the ground level eventually depend on the full falling history and on all the microphysical interactions happening “from the cloud to the ground”.

The shape, density, and growth rate of individual crystals is mostly a function of temperature and relative humidity of the environment in which they form (Magono and Lee, 1966; Chen and Lamb, 1994; Fukuta and Takahashi, 1999; Bailey and Hallett, 2009; Takahashi, 2014). Individual crystals can branch together (aggregation) and/or collect supercooled liquid water droplets that freeze upon impact on the surface of the crystals (riming) that are in this way accreted. In contrast to aggregation, riming leads a net increase of the mass of precipitation. This happens because the rimed crystals or snowflakes have much larger fall velocities than individual water droplets in supercooled liquid water clouds, that would otherwise not be able to reach the ground at a significant rate. Aggregation indirectly contributes to the mass transfer by generating larger and faster targets for riming (Houze and Medina, 2005, hereafter HM2005).

Riming is more efficient on large crystals (Ono, 1969), even though it was recently shown that the process can also occur on very small crystals, with characteristic dimensions as small as 60  $\mu\text{m}$  (Avila et al., 2009). Turbulence and vertical air motion (updraft) contribute significantly to riming. Turbulence influences the motion of ice crystal leading to larger droplet collection volumes and therefore to large collection efficiencies (Pinsky and Khain, 1998). Updraft, in turn, is necessary to sustain the production of SLW (Rauber and Tokay, 1991).

The impact of riming on the bulk properties of snowfall is critical. Measurements of freshly fallen snow, both in the Sierra Nevada (US) and in the proximity of Sapporo (Japan), showed that 30 to 60% of the total mass of snowfall is constituted by frozen SLW droplets on the snowflakes, also called rimed accretion (Harimaya and Sato, 1989; Mitchell et al., 1990). Additionally, the accumulation of rimed snowflakes on the ground is more prone to generate instabilities and to initiate avalanches (Abe, 2004). A last aspect to consider is that, during precipitation, riming can be associated with ice splintering and thus to (secondary) ice generation. The most known example of secondary ice production is the Hallet-Mossop ice multiplication mechanism (Hal-

Riming in winter alpine snowfall during CLACE 2014

J. Grazioli et al.

Title Page

Abstract

Introduction

Conclusions

References

Tables

Figures



Back

Close

Full Screen / Esc

Printer-friendly Version

Interactive Discussion



## Riming in winter alpine snowfall during CLACE 2014

J. Grazioli et al.

Title Page

Abstract

Introduction

Conclusions

References

Tables

Figures



Back

Close

Full Screen / Esc

Printer-friendly Version

Interactive Discussion



lett and Mossop, 1974) occurring at temperatures higher than  $-8^{\circ}\text{C}$  on heavily rimed hydrometeors. However, other mechanisms exist to explain secondary ice generation at colder temperatures. One example is constituted by ice-to-ice and ice-to-water collisional mechanisms (Vardiman, 1978; Yano and Phillips, 2011), that are in any case favoured by the degree of riming of the colliding crystals. Non-collisional mechanisms have been hypothesized as well. For instance Rangno (2008) described the process of fragmentation of freezing supercooled droplets in mixed phase clouds and recently Lloyd et al. (2015) hypothesized that the lifting and transport of hoarfrost crystals from the ground to the clouds could explain the very high concentration of small crystals frequently observed in winter clouds.

Dual-polarization Doppler (polarimetric) weather radars operating at microwave frequencies are becoming state-of-the-art instruments to document the microphysics of ice-phase precipitation. These systems are able to provide indirect information about size, intensity, geometry, density, velocity and turbulence of falling hydrometeors (e.g. Bringi and Chandrasekar, 2001; Doviak and Zrnić, 2006). Polarimetric data have been used to identify areas of intense growth of dendritic and planar crystals (Kennedy and Rutledge, 2011; Bechini et al., 2013) and to formulate hypotheses on the dominant microphysical processes occurring over vertical columns of snowfall (Schneebeli et al., 2013; Andric et al., 2013; Kumjian et al., 2014). The combination of numerical modelling, radar observations and in-situ data led to the development of classification methods able to estimate the type of hydrometeors that populate individual radar resolution volumes (e.g. Straka et al., 2000; Dolan and Rutledge, 2009; Bechini and Chandrasekar, 2015; Grazioli et al., 2015). However, the complex microphysics of ice-phase precipitation cannot be fully captured by polarimetric radars alone. Combinations of remote sensing with in-situ instruments have shown to be useful and often necessary to characterize at the same time precipitation, clouds, and environmental conditions (Hogan et al., 2002, 2003; Bechini et al., 2013, hereafter BBC2013). Despite several years of research and technological development, many microphysical processes of winter precipitation in complex terrains remain not fully understood, including the

relation between snowfall intensity and degree of riming or the conditions leading to efficient generation of rimed precipitation.

This manuscript presents results of an investigation into the relation between riming and snowfall intensity, the temporal evolution and the vertical structure of intense winter precipitation events originating in mixed-phase clouds based on polarimetric radar and in-situ observations collected during winter alpine snowfall. The manuscript is structured as follows: Sect. 2 provides information about the main instrumental set up. Section 3 presents the analyses that relate rimed precipitation with snow accumulation as well as a microphysical description of the vertical structure of precipitation. Section 4 is devoted to the detailed description of a particularly intense snowfall event characterized by a persistent turbulent layer driven by wind shear, and Sect. 5 summarizes the main results and provides conclusions and perspectives.

## 2 Measurement campaign and instruments

The major part of the measurements shown in this manuscript were collected during the Cloud and Aerosol Characterization Experiment (CLACE), occurring in January and February 2014. CLACE takes place yearly in the central Alps of Switzerland, in various measurements sites located above 2000 m (e.g. Zieger et al., 2012).

### 2.1 Instruments

Figure 1 shows the location of the three main measurement sites considered in the present work: Kleine Scheidegg (KS, 2061 m), Männlichen (MAE, 2230 m), and Jungfrauoch (JFJ, 3580 m). The topography of the measurement area is very complex, with mountain peaks above 4000 m and steep elevation gradients.

## Riming in winter alpine snowfall during CLACE 2014

J. Grazioli et al.

Title Page

Abstract

Introduction

Conclusions

References

Tables

Figures



Back

Close

Full Screen / Esc

Printer-friendly Version

Interactive Discussion



## 2.1.1 Kleine Scheidegg (KS)

A polarimetric Doppler weather radar was deployed at the KS location. The system, named MXPoI, is an X-band (3.2 cm wavelength) radar with angular resolution of about 1.5° and range resolution of 75 m (complete specifications are given in Schneebeli et al., 2013; Scipion et al., 2013). MXPoI provides as main products the horizontal reflectivity factor  $Z_H$  [dBZ], differential reflectivity  $Z_{DR}$  [dB], copolar cross correlation coefficient  $\rho_{hv}$ , specific differential phase shift upon propagation  $K_{dp}$  [° km<sup>-1</sup>], mean Doppler velocity  $v$  [m s<sup>-1</sup>] and Doppler spectrum width  $\sigma_v$  (Doviak and Zrnić, 2006). A hydrometeor classification method (Grazioli et al., 2015, hereafter, GTB2015) was developed based on clustering techniques and applied to the polarimetric data. GTB2015 classifies dry snowfall into three broad categories: aggregates (AG), individual crystals (CR), rimed ice particles (RI).

During CLACE 2014, MXPoI was operating with a scanning sequence of about 4.5 min, repeated indefinitely. In this manuscript we will employ Plan Position Indicator (PPI) scan data collected at an elevation of 10° over the Grindelwald valley (≈ 45° North-East of KS in Fig. 1), Range Height Indicator (RHI) scans collected over the Grindelwald valley and vertical profiles (25 s duration) collected three times during each sequence. The maximum range distance sampled by MXPoI during CLACE was about 20 km.

## 2.1.2 Männlichen (MAE)

At the MAE site, snow height on the ground was measured by an automatic station whose data are made available by MeteoSwiss. Time series of snow height measurements in time are used to quantify snow accumulations and accumulation rates of the precipitation events. Among other gauging stations in this area, MAE is chosen because: (i) it provides relatively high resolution data (30 min), (ii) it is among the closest to KS, (iii) it is located approximately at the altitude of the first radar resolution volume not affected by ground clutter and radar blind range.

### 2.1.3 Jungfraujoch (JFJ)

The JFJ observatory is a known site for atmospheric studies of aerosols and clouds (e.g. Baltensperger et al., 1997) and during CLACE 2014 it accommodated several sensors. The ones that are of direct interest for the present work are listed here. A weather station managed by MeteoSwiss provided general meteorological information and a sonic anemometer provided high resolution wind information. A Cloud Droplet Probe (CDP-100, Lance et al., 2010) yielded quantification of SLW content. CDP measures the light scattered by droplets and determines the optical equivalent diameter over the size range 2 to 50  $\mu\text{m}$  at a 1 Hz acquisition frequency. A 3-View Cloud Particle Imager (3V-CPI) provided images and habits of liquid and ice-phase hydrometeors in the 10 to 1280  $\mu\text{m}$  size range. This instrument is the combination of a Two-Dimensional Stereoscopic (2D-S, Lawson et al., 2006) laser shadow imaging probe and of a high frame rate Cloud Particle Imager (CPI Model 2) probe. The 2D-S component of the 3V-CPI instrument was used to analyse particle imagery in order to produce information on the concentration, size and phase of cloud particles.

The in-situ sensor at the JFJ site and the polarimetric radar (KS site, Fig. 1), both continuously acquiring data, allow the contextualization of radar observations with respect to the cloud conditions over long time intervals. This is a definite added value of CLACE 2014. Similar comparisons between radars and cloud probes have in fact otherwise been performed only on limited time intervals, the cloud probes being usually aircraft-borne (e.g. Hogan et al., 2002, 2003; Houze and Medina, 2005).

### 2.2 Precipitation events

The months of January and February 2014 were relatively rich in terms of precipitation. By means of visual inspection of all the observations collected by MXPoI, 13 precipitation events occurring in the measurement domain have been identified. These events have been summarized in Table 1. One event (event 9 in the table) is listed for the sake of completeness but it will not be included in the following analysis. In this specific case

## Riming in winter alpine snowfall during CLACE 2014

J. Grazioli et al.

Title Page

Abstract

Introduction

Conclusions

References

Tables

Figures



Back

Close

Full Screen / Esc

Printer-friendly Version

Interactive Discussion







vals and not during the entire precipitation event. In this section we will analyse the most representative time steps identified by GTB2015 as rimed precipitation and we will compare the measurements of MXPoI with the in-situ information of the instruments deployed at JFJ.

The most representative cases in this sense are identified by means of the following constraints: (i) duration of at least half a hour, (ii) average PRP above 50 % (calculated over the whole vertical column), (iii) peaks of at least 15 min characterized by PRP greater than 75 % for all the altitudes below the JFJ. The first constraint is justified by the need of collecting a statistically significant number of radar observations at the JFJ height (over a domain of approximately 20 km) to be compared with the in-situ measurements of much higher temporal resolution but collected at a single location. The second constraint ensures that riming is the actual dominant process, as classified by GTB2015, while the third one ensures that a large amount of rimed precipitation is also reaching the ground level.

Figure 4 summarizes the global characteristics of the 6 representative cases isolated in this way. These events are named after the time interval of Table 1 they belong to and they are listed in Table 2. Panel a puts these cases into a context of snow accumulation. All the cases in the figure, with the exception of EV4, exhibit above-average snowfall intensities. One of them in particular, EV3, is standing out because only 2.5 % of the snowfall time intervals of the same duration occurring during the winter seasons (October–April) from 2000 to 2014 had higher intensities. Panel b is used to show, for each case, average vertical profiles of PRP and to highlight the relative position of the JFJ (indicated by a dashed black line) within each snow storm. During EV3, EV4, EV6 and EV7, JFJ is situated in the upper edge of the vertical column of rimed precipitation and in the present section we will refer to them as “core events”. On the contrary, during EV5 and EV13, JFJ is located above the “rimed core” and we will refer to them as “edge events”.

Now that the selected cases have been put into context we shall proceed to analyse their characteristics by means of radar observations and in-situ measurements. Each

## Riming in winter alpine snowfall during CLACE 2014

J. Grazioli et al.

[Title Page](#)[Abstract](#)[Introduction](#)[Conclusions](#)[References](#)[Tables](#)[Figures](#)[Back](#)[Close](#)[Full Screen / Esc](#)[Printer-friendly Version](#)[Interactive Discussion](#)

case of interest, that we will refer to as “rimed phase”, is compared with a reference time interval covering the 3 previous hours, named “preceding phase”. Such comparison is shown in Figs. 5 and 6. Figure 5 illustrates the behaviour of variables related to wind and turbulence while Fig. 6 illustrates the evolution of radar horizontal reflectivity  $Z_H$  and in-situ LWC during the selected cases.

### 3.2.1 Edge events (EV5, EV13)

EV5 and EV13 have been sampled, from the JFJ perspective, above the actual “rimed core” of precipitation (see Fig. 4b). We can observe in Fig. 6b that they show the lowest  $Z_H$  values at the JFJ height during the rimed phase of the event. As  $Z_H$  in our observations increases with decreasing altitude, these two events are sampled closer to the cloud top than the other ones. Therefore the in-situ measurements provide in this case information about the processes occurring at the highest levels of rimed precipitation. Liquid water is available during both events (Fig. 6b), in much higher concentration during EV13 and it is not depleted as the event evolves.

### 3.2.2 Core events (EV3, EV4, EV6, EV7)

The “core” events are of major interest for the microphysical descriptions presented in the present paper. EV6 and EV7 behave similarly in terms of evolution of wind and turbulence (Fig. 5). In both cases the preceding phase (red histograms) is observed to be more turbulent than the rimed phase (blue histograms). All the variables shown in this figure are decreasing during the transition between the two phases. Doppler spectral width, shown in panel a, reduces of about 50 %, as well as the wind speed (panel c). The Doppler velocity (panel b), influenced by particle fall velocity and air motion, shows positive values (particles updraft) and in general a larger variability during the preceding phase. It can be hypothesized that the turbulent part of the events creates the appropriate conditions to generate rimed precipitation, that falls out efficiently during the following calmer part. Turbulence, and in particular updraft are in fact im-

## Riming in winter alpine snowfall during CLACE 2014

J. Grazioli et al.

Title Page

Abstract

Introduction

Conclusions

References

Tables

Figures



Back

Close

Full Screen / Esc

Printer-friendly Version

Interactive Discussion



portant factors leading to riming by providing SLW droplets and conditions that favour collision (Raubert and Tokay, 1991; Pinsky and Khain, 1998; Houze and Medina, 2005).

As observed in Fig. 6, during EV7 the liquid water content is always low, before and during the rimed phase, leading us to believe that in this case riming occurred at much higher altitudes. In favour of this hypothesis there is the significant vertical extension of this snowfall event, as shown in Fig. 4b, with respect to the other ones. EV6 exhibits a very interesting LWC trend. LWC is practically entirely depleted before the rimed phase, with a transition of maximum values from around  $0.45 \text{ gm}^{-3}$  to around  $0.05 \text{ gm}^{-3}$ . We believe that this is the actual signature of the efficient mass transfer due to riming, from the liquid mass suspended in the clouds to the ice mass that precipitates. In the rimed phase of the event, the LWC is collected in the form of rimed accretion, especially on the largest precipitating hydrometeors and therefore it is not available any more in the form of water droplets.

The trends of EV4 are similar to EV6, even though the magnitude of the variables is very different. Also in this case a decrease of turbulence (except for the spectral width) and wind intensity (Fig. 5) can be observed, as well as a decrease of LWC (Fig. 6a) in the transition between the preceding phase and rimed phase. Wind intensities remain extremely high, with the 5 % quantile never below  $16 \text{ ms}^{-1}$ . Such wind intensities affect the snowfall flux towards the ground and introduce significant uncertainty on snow accumulation measurements. This probably explains why this case did not generate any significant response in terms of snowfall accumulation (Fig. 4a).

EV3 is probably the most interesting one because it shows opposite trends with respect to EV6 and EV7. Notably, LWC is this time higher in the rimed part of the event (Fig. 6a) while turbulence and wind intensity remain almost constant. This case, occurring during the event number 3 of Table 1, was lasting about 9 h, was about three times longer than the second longest “rimed” case, and it had an average snowfall intensity of more than  $2.1 \text{ cm h}^{-1}$ . This value represents a very high quantile of snowfall intensity in comparison with events of analogous duration in the same area (Fig. 4). For these reasons it will be further discussed in the next sections.

Riming in winter  
alpine snowfall  
during CLACE 2014

J. Grazioli et al.

Title Page

Abstract

Introduction

Conclusions

References

Tables

Figures



Back

Close

Full Screen / Esc

Printer-friendly Version

Interactive Discussion





## Riming in winter alpine snowfall during CLACE 2014

J. Grazioli et al.

Title Page

Abstract

Introduction

Conclusions

References

Tables

Figures



Back

Close

Full Screen / Esc

Printer-friendly Version

Interactive Discussion



shape enhancement (Takahashi, 2014; Andric et al., 2013). The enhancement is in this case moderate, with peak values mostly below 1 dB suggesting that depositional growth is not the only process taking place. In fact,  $Z_{DR}$  is largely influenced by the geometry of the particle that contribute the most to the  $Z_H$  signal (i.e. the biggest ones, Hubbert et al., 2014) such that the presence of even a few large isotropic aggregates significantly decreases  $Z_{DR}$ .

The peak of  $K_{dp}$ , below altitudes of higher  $Z_{DR}$  and above altitudes of higher  $Z_H$ , is a well known but still not completely understood signature observed during snowfall (Kennedy and Rutledge, 2011; Bechini et al., 2013; Andric et al., 2013; Hubbert et al., 2014). The proximity of this signature with respect to the  $-15^\circ\text{C}$  level (blue line in Fig. 7) has lead in the past to associate it to dendritic crystal growth (Kennedy and Rutledge, 2011). However, it was recognized that the concentration of dendrites needed to generate enhancements of this magnitude would lead to unreasonably high values of  $Z_H$  when these crystals eventually aggregate (Andric et al., 2013). It has been demonstrated that the particles responsible of this signatures must be small compared to the radar wavelength as they were shown to behave as Rayleigh scatterers by BBC2013 and Hubbert et al. (2014). BBC2013 and A2013 proposed two interesting and not mutually exclusive explanations. BBC2013 hypothesized that rimed dendrites would be able to generate such significant  $K_{dp}$  enhancement.  $K_{dp}$  is in fact, with other conditions fixed, increasing with the density of the ice particles. A2013 suggested instead that secondary ice production of very small oblate crystals would need to take place, either as a result of splintering (Hallett and Mossop, 1974, or other multiplication mechanisms) or as a result of direct nucleation from the liquid phase with a similar process as described in Westbrook and Illingworth (2011).

In the end, both hypotheses describe by-products of the riming process and our interpretation is that the enhancement of  $K_{dp}$  in this region is probably the radar signature of riming. From one side, riming of already existing anisotropic crystals would enhance their contribution to  $K_{dp}$  by increasing the particle density and thus the dielectric response. From the other side, the formation of secondary ice can follow as

## Riming in winter alpine snowfall during CLACE 2014

J. Grazioli et al.

Title Page

Abstract

Introduction

Conclusions

References

Tables

Figures



Back

Close

Full Screen / Esc

Printer-friendly Version

Interactive Discussion



well the mechanisms of Vardiman (1978) or Yano and Phillips (2011): less efficient, not constrained by temperature, but always favoured by riming or the recently proposed mechanism of hoarfrost crystals lifting and transport (Lloyd et al., 2015). In the latter cases the increase of  $K_{dp}$  is driven mostly by the number concentration of ice crystals.

5 During EV3, EV6, and EV7, the measurements of LWC and the turbulent conditions, as well as the radar-based classification (see Sect. 3.2) led us to a confident identification of riming at these altitude levels. Figure 8 displays the type of particles in the size range 10 to 1280  $\mu\text{m}$  recorded at the level of the JFJ by the 2D-S instrument, for EV3, EV6, and EV7 respectively (at the same time-steps shown in Fig. 7). We observe  
 10 during EV6 and EV7 the presence of heavily rimed particles with non recognizable original shape as well as of rimed particles probably originating from planar crystals. The ice particles number concentrations measured around these time steps ranged from 5 to 20  $\text{L}^{-1}$  with modal values around 10  $\text{L}^{-1}$  for EV6 and from 5 to 23  $\text{L}^{-1}$  with modal values around 10  $\text{L}^{-1}$  for EV7<sup>1</sup>. The mean mass of the crystals in the size range  
 15 sampled (obtained by dividing the total 2D-S ice mass content by the ice number concentration) during these time intervals was about 10 and 6  $\mu\text{g}$  during EV6 and EV7, respectively. On the contrary, during EV3 rimed crystals are observed together with a large amount of small particles (some of them highly oblate), of various shapes. The ice number concentration around this time step ranged from 25 to 100  $\text{L}^{-1}$  with modal values around 50  $\text{L}^{-1}$  (larger than the case of EV6 and EV7) and the mean mass of the ice crystals was about 3.5  $\mu\text{g}$ . We can hypothesize that during EV6 and EV7 the  $K_{dp}$  signal is generated mostly by heavier riming of larger anisotropic crystals (but still in the Rayleigh regime) while during EV3 it results from the higher concentration of smaller oblate particles. This also is confirmed by the higher values of  $Z_{DR}$  during EV6  
 20 and EV7 especially, at this altitude, if we recall that  $Z_{DR}$  is mostly influenced by the oblateness of larger particles. It is also worth noting, by looking at the particle images of Fig. 8 (and many others not shown here) that the  $K_{dp}$  enhancement seems not to

<sup>1</sup>These are reference values calculated within a 10 min time window. The given range of variation is based on 5 and 95 % quantile.



## 4 Case study (EV3): turbulence, wind shear, and snowfall enhancement

### 4.1 Detailed description of EV3

We shall now come back to the peculiar case of EV3. EV3 occurred during the precipitation event leading to the largest snow accumulation (Fig. 3). There was an average precipitation intensity of  $2.1 \text{ cm h}^{-1}$  for a 9 h duration. Over the past 14 years, less than 2.5% of snowfall cases of this duration (in the same location) led to higher intensities. As documented in Fig. 6, SLW droplets were available during the whole event and they were not rapidly depleted as happened in other cases. It is therefore instructive to investigate which mechanisms sustained the production of SLW and the significant snowfall. From the observations of Fig. 7, the vertical structure of EV3 appeared similar to the other “rimed” cases in terms of polarimetric variables. However, by looking at the average vertical structure of two Doppler-related radar variables (Doppler velocity and Doppler spectral width at vertical incidence) for the six cases of Table 2, an obvious difference emerges (Fig. 10). EV6, EV7, EV8 and EV13 do not exhibit particular signatures: the distribution of Doppler velocities is globally narrow and the occurrence of updrafts (positive values of Doppler velocity at vertical incidence) is very limited. Doppler spectral width values are lower than  $1 \text{ ms}^{-1}$ , with median values always lower than  $0.5 \text{ ms}^{-1}$ . EV4 on the contrary is extremely turbulent over the whole range of heights: even at the lowest heights updrafts are frequent and over all the heights values of spectral width up to  $3 \text{ ms}^{-1}$  are observed. EV3, finally, shows a peculiarity: the turbulence in this case appeared to be confined between approximately 3000 and 4000 m. In this layer the spectral width reaches values up to  $2.5 \text{ ms}^{-1}$  and updrafts are observed, while at altitudes below 3000 m the range of velocities and spectral width is similar to other events.

The synoptic situation occurring on the 1 February at 12:00 UTC, just a few hours before the beginning of EV3, is represented in Fig. 11. The 500 hPa geopotential height (panel a) shows the presence of a deep trough extending from the British Isles to Western Europe, approaching the Alpine slopes from the West. Such synoptic con-

**Riming in winter  
alpine snowfall  
during CLACE 2014**

J. Grazioli et al.

Title Page

Abstract

Introduction

Conclusions

References

Tables

Figures



Back

Close

Full Screen / Esc

Printer-friendly Version

Interactive Discussion



figuration has been already identified as responsible for heavy snowfalls in the alpine regions (Panziera and Hoskins, 2008). A cold front was associated with the trough, as is clearly visible from the 850 hPa temperature shown in panel b. The atmospheric sounding of Payerne (Lat. 46.82, Lon. 6.94) at 12:00 UTC, not shown here, indicates the presence of a strong south-westerly flow above 2 km. A South-Westerly low-level jet was also observed between 1 and 1.3 km. The sounding of the 2 February at 00:00 UTC (not shown) reveals that after the passage of the cold front the temperature decreased by more than 10 °C at an altitude of about 2 km over Payerne, consistent with the constant temperature drop which was also observed at the JFJ station in the afternoon. The passage of the cold front occurred between 21:00 and 00:00 UTC, as clearly shown by the measurements of atmospheric pressure collected at the JFJ (see Fig. 12b), and by the sharp change in wind direction observed in Gütsch (Lat. 46.65, Lon. 8.61, alt. 2283 m), a nearby meteorological station not influenced by wind channelling as is the JFJ. The cold front produces a significant and steady accumulation of snowfall at the ground level in MAE, as shown in Fig. 12a.

Figure 10 reveals the presence of a turbulent layer between 3000 and 4000 m of altitude at the temporal scale of the entire duration of EV3. Figures 13 and 14 illustrate the dynamics of EV3 in a more complete and dynamic way. Figure 13a depicts the vertical structure of Doppler spectral width: the turbulent layer is clearly visible at the expected altitudes and it is relatively stable in time. In Fig. 13b, showing the Doppler velocity at vertical incidence, we observe frequent updrafts within the turbulent layer. Figure 13c shows for each height and time the mean value of Doppler velocity measured within a radar RHI scan. Each vertical cut of this kind of plot is the summary of an entire RHI scan. Such RHI-derived plots do not consider RHI elevations angle higher than 45° in order to preserve polarimetric signals and horizontal wind components. In this case we observe that the turbulent layer is caused by wind shear: two air masses with different relative motion with respect to the radar location are in contact. The change of sign of the Doppler velocities from negative to positive happens at the top of the turbulent layer, where the two air masses are mixing. Because the JFJ is sit-



## Riming in winter alpine snowfall during CLACE 2014

J. Grazioli et al.

Title Page

Abstract

Introduction

Conclusions

References

Tables

Figures



Back

Close

Full Screen / Esc

Printer-friendly Version

Interactive Discussion



The effect of wind shear and turbulent recirculation on the microphysics of snowfall has been observed by Hogan et al. (2002), hereafter H2002. Also in this case, the large scale conditions and geographical locations described in H2002 are very different with respect to CLACE 2014. However, the microphysical processes described may also occur in alpine regions. In particular H2002 explained that wind shear and updrafts together continuously feed the regions above the shear layer with SLW and ice fragments (generated by secondary ice production mechanisms) and favour the growth of anisotropic ice crystals at this level. This phenomenon creates an enhancement of  $Z_{DR}$ , very similar to what we observe in our case in Fig. 14c. Additionally, H2002 recognized that secondary ice, by-product of the riming process, can be recirculated in the layer of shear and grow into oblate small ice particles like the ones that we can observe in Fig. 8. This mechanism, resulting in increased concentration of particles, can explain the enhancement of  $K_{dp}$  observed within the turbulent layer. It is worth noting that  $K_{dp}$  was unfortunately not available in the study of H2002. This parameter has the definite advantage over  $Z_{DR}$  of being unbiased by the presence of large isotropic particles (like aggregates) that unavoidably are formed in areas of turbulent mixing. Regarding the generation of secondary ice, H2002 presented evidence for a Hallett-Mossop mechanism (Hallett and Mossop, 1974), that occurs at temperatures warmer than  $-8^{\circ}\text{C}$ . The enhancement of  $K_{dp}$  happens in our case at lower temperatures and this leads us to assume that other ice production mechanisms may be taking place. A first possible explanation would involve collisional mechanisms (e.g. Vardiman, 1978; Yano and Phillips, 2011) that require only earlier stages of riming, presence of supercooled liquid water, ice crystals, and turbulence (all conditions that are met during EV3). A second explanation, recently proposed for the same measurement campaign of CLACE 2014 (Lloyd et al., 2015), would be the lifting and transport of hoarfrost crystals generated at the ground level. During EV3 the environmental conditions are favourable to this process: wind and turbulence are significant (Fig. 5) and the main direction of propagation of the incoming front (South-Westerly) leads the precipitation system to interact at first with

the highest peaks in the region (Fig. 1), while the radar and in-situ measurements are collected downwind (leeward) from them.

Figure 15 summarizes schematically the possible role that the turbulent layer was playing during EV3. Above the layer (enhanced  $Z_{DR}$ ) favourable conditions exist for anisotropic crystal growth thanks to the recirculation of SLW and ice fragments from the lower levels. Within the turbulent layer, aggregation and riming are initiated. Both riming itself and the availability of large quantities of small crystals, likely deriving from collisional ice multiplication, contribute to the peak of  $K_{dp}$ . Aggregation and size sorting (e.g. Dawson et al., 2015) result in an increase of  $Z_H$  in the bottom part of the turbulent layer. Aggregation and further riming will then continue to raise  $Z_H$  until precipitation reaches the ground. In this global view, precipitation will be enhanced as long as the turbulent layer persists.

## 5 Summary and conclusions

This manuscript presented polarimetric radar and in-situ measurements of precipitation in a mixed-phase cloud environment during CLACE 2014, in the central Alps of Switzerland. It was shown, thanks to the comparison between radar-based hydrometeor classification and measurements of snow accumulation, that riming is a leading factor to explain large values of snow accumulation. The parts of the precipitation events that exhibited significant riming have been further analysed. Most of the time, radar observations of rimed precipitation were following time periods of enhanced turbulence and availability of SLW. When rimed precipitation was most intense, instead, the turbulence was usually lower (thus favouring the precipitation) and SLW was depleted in the cores of rimed precipitation, being probably collected in the form of rimed accretion on the precipitating ice crystals. One noteworthy exception was constituted by a snowfall event named EV3 (statistically, the most intense one). In this case, a stable layer of wind-shear driven turbulence, associated with the passage of a cold front, created favourable conditions for the sustained production of SLW, ice-to-ice interac-

## Riming in winter alpine snowfall during CLACE 2014

J. Grazioli et al.

Title Page

Abstract

Introduction

Conclusions

References

Tables

Figures



Back

Close

Full Screen / Esc

Printer-friendly Version

Interactive Discussion



tion, and efficient fallout of water masses by means of a mechanism similar to what presented in Houze and Medina (2005). A microphysical interpretation of this mechanism has been proposed: anisotropic crystal growth dominates the areas just above the turbulent layer while riming and aggregation are favoured by the turbulent interactions.

The vertical structure of the events during which riming was significant has been examined by means of the radar polarimetric variables and in-situ ice particle probes. A common feature of these cases was shown to be a peak of  $K_{dp}$ , associated either with relatively large concentrations of small ice crystals (probably associated with secondary ice generation or hoarfrost ice transport) or with the riming of ice crystals with anisotropic shapes. The enhancement of  $K_{dp}$  has been shown to be related to the maximum  $Z_H$  measured in the vertical column of precipitation. Even though previous studies hypothesized the  $K_{dp}$  signature to be associated with dendritic growth, particle images (limited however to 1.28 mm of maximum sampling size) collected within this area of the storm did not show any evident or dominant pristine and unrimed crystal habit in these cases.

The present study provided insight about the relation between riming and snow accumulation, the microphysics of riming, and the potential role of sustained turbulence on snowfall generation. It also illustrated the complementarity of in-situ and remote sensing instruments for the description of snowfall microphysics in complex terrain. Future studies should include radar measurements at higher frequencies, to better capture the transition between clouds and precipitation, and in-situ particle imagers of larger maximum sampling size in order to visualize the hydrometeors that contribute most to the total  $Z_H$  signal and that are larger targets for riming. The potential role of turbulence in the microphysics and accumulation of snow should be further investigated, in order to understand if the patterns described for EV3 are recurring.

*Acknowledgements.* We are grateful to Erik Herrmann and to Christopher Hoyle of the Paul Scherrer Institut for the organization of CLACE 2014. For the field deployment and maintenance of the instruments we thank Daniel Wolfensberger and Tim Raupach (EPFL-LTE) as well as all those people of the Jungfrau railway and sky resort that assisted us during the installation of

the radar. Many meteorological datasets have been provided by MeteoSwiss, the Swiss Federal Office of Meteorology and Climatology.

## References

- Abe, O.: Shear strength and angle of repose of snow layers including graupel, in: *Annals of Glaciology*, vol. 38, Int. Glaciol Soc., Swiss Fed Inst. Snow & Avalanches, Davos, Switzerland, 305–308, doi:10.3189/172756404781815149, 2004. 18067
- Andric, J., Kumjian, M. R., Zrnica, D. S., Straka, J. M., and Melnikov, V. M.: Polarimetric signatures above the melting layer in winter storms: an observational and modeling study, *J. Appl. Meteorol. Clim.*, 52, 682–700, doi:10.1175/JAMC-D-12-028.1, 2013. 18068, 18077, 18078
- Avila, E. E., Castellano, N. E., Saunders, C. P. R., Buergesser, R. E., and Aguirre Varela, G. G.: Initial stages of the riming process on ice crystals, *Geophys. Res. Lett.*, 36, L09808, doi:10.1029/2009GL037723, 2009. 18067
- Bailey, M. P. and Hallett, J.: A comprehensive habit diagram for atmospheric ice crystals: confirmation from the laboratory, AIRS II, and other field studies, *J. Atmos. Sci.*, 66, 2888–2899, doi:10.1175/2009JAS2883.1, 2009. 18067
- Baltensperger, U., Gaggeler, H. W., Jost, D. T., Lugauer, M., Schwikowski, M., Weingartner, E., and Seibert, P.: Aerosol climatology at the high-alpine site Jungfrauoch, Switzerland, *J. Geophys. Res.-Atmos.*, 102, 19707–19715, doi:10.1029/97JD00928, 1997. 18071
- Bechini, R. and Chandrasekar, V.: A semisupervised robust hydrometeor classification method for dual-polarization radar applications, *J. Atmos. Ocean. Tech.*, 32, 22–47, doi:10.1175/JTECH-D-14-00097.1, 2015. 18068
- Bechini, R., Baldini, L., and Chandrasekar, V.: Polarimetric radar observations in the ice region of precipitating clouds at C-band and X-band radar frequencies, *J. Appl. Meteorol. Clim.*, 52, 1147–1169, doi:10.1175/JAMC-D-12-055.1, 2013. 18068, 18078
- Bringi, V. N. and Chandrasekar, V.: *Polarimetric doppler weather radar*, Cambridge University Press, doi:10.1017/CBO9780511541094, 2001. 18068
- Cantrell, W. and Heymsfield, A.: Production of ice in tropospheric clouds, *B. Am. Meteorol. Soc.*, 86, 795–897, doi:10.1175/BAMS-86-6-795, 2005. 18066

## Riming in winter alpine snowfall during CLACE 2014

J. Grazioli et al.

Title Page

Abstract

Introduction

Conclusions

References

Tables

Figures



Back

Close

Full Screen / Esc

Printer-friendly Version

Interactive Discussion



**Riming in winter  
alpine snowfall  
during CLACE 2014**

J. Grazioli et al.

Title Page

Abstract

Introduction

Conclusions

References

Tables

Figures



Back

Close

Full Screen / Esc

Printer-friendly Version

Interactive Discussion



Chen, J. P. and Lamb, D.: The theoretical basis for the parametrization of ice crystal habits – growth by vapor-deposition, *J. Atmos. Sci.*, 51, 1206–1221, doi:10.1175/1520-0469(1994)051<1206:TTBFTP>2.0.CO;2, 1994. 18067

Colle, B. A., Stark, D., and Yuter, S. E.: Surface microphysical observations within east coast winter storms on Long Island, New York, *Mon. Weather Rev.*, 142, 3126–3146, doi:10.1175/MWR-D-14-00035.1, 2014. 18072, 18095

DDawson II., D. T., Mansell, E. R., and Kumjian, M. R.: Does wind shear cause hydrometeor size sorting?, *J. Atmos. Sci.*, 72, 340–348, doi:10.1175/JAS-D-14-0084.1, 2015. 18085

Dolan, B. and Rutledge, S. A.: A theory-based hydrometeor identification algorithm for X-band polarimetric radars, *J. Atmos. Ocean. Tech.*, 26, 2071–2088, doi:10.1175/2009JTECHA1208.1, 2009. 18068, 18073

Doviak, R. and Zrnić, D.: *Doppler Radar and Weather Observations*, 2nd edn., Dover Publications, San Diego, 2006. 18068, 18070

Fukuta, N. and Takahashi, T.: The growth of atmospheric ice crystals: a summary of findings in vertical supercooled cloud tunnel studies, *J. Atmos. Sci.*, 56, 1963–1979, doi:10.1175/1520-0469(1999)056<1963:TGOAIC>2.0.CO;2, 1999. 18067

Grazioli, J., Tuia, D., and Berne, A.: Hydrometeor classification from polarimetric radar measurements: a clustering approach, *Atmos. Meas. Tech.*, 8, 149–170, doi:10.5194/amt-8-149-2015, 2015. 18068, 18070, 18073

Hallett, J. and Mossop, S. C.: Production of secondary ice particles during the riming process, *Nature*, 249, 26–28, doi:10.1038/249026a0, 1974. 18067, 18078, 18084

Harimaya, T. and Sato, Y.: Measurement of the riming amount on snowflakes, *J. Fac. Sci. Hokkaido Univ.*, 8, 355–366, 1989. 18067, 18072

Hogan, R. J., Field, P. R., Illingworth, A. J., Cotton, R. J., and Choulaton, T. W.: Properties of embedded convection in warm-frontal mixed-phase cloud from aircraft and polarimetric radar, *Q. J. Roy. Meteor. Soc.*, 128, 451–476, doi:10.1256/003590002321042054, 2002. 18068, 18071, 18084

Hogan, R. J., Francis, P. N., Flentje, H., Illingworth, A. J., Quante, M., and Pelon, J.: Characteristics of mixed-phase clouds. I: Lidar, radar and aircraft observations from CLARE'98, *Q. J. Roy. Meteor. Soc.*, 129, 2089–2116, doi:10.1256/qj.01.208, 2003. 18068, 18071

Houze, R. A. and Medina, S.: Turbulence as a mechanism for orographic precipitation enhancement, *J. Atmos. Sci.*, 62, 3599–3623, 2005. 18067, 18071, 18072, 18076, 18080, 18086

---

**Riming in winter  
alpine snowfall  
during CLACE 2014**

---

J. Grazioli et al.

[Title Page](#)[Abstract](#)[Introduction](#)[Conclusions](#)[References](#)[Tables](#)[Figures](#)[Back](#)[Close](#)[Full Screen / Esc](#)[Printer-friendly Version](#)[Interactive Discussion](#)

- Hubbert, J. C., Ellis, S. M., Chang, W. Y., Rutledge, S., and Dixon, M.: Modeling and interpretation of S-band ice crystal depolarization signatures from data obtained by simultaneously transmitting horizontally and vertically polarized fields, *J. Appl. Meteorol. Clim.*, 53, 1659–1677, doi:10.1175/JAMC-D-13-0158.1, 2014. 18078
- 5 Kennedy, P. C. and Rutledge, S. A.: S-band dual polarization radar observations of winter storms, *J. Appl. Meteorol. Clim.*, 50, 844–858, doi:10.1175/2010JAMC2558.1, 2011. 18068, 18078
- Kumjian, M. R., Rutledge, S. A., Rasmussen, R. M., Kennedy, P. C., and Dixon, M.: High-resolution polarimetric radar observations of snow-generating cells, *J. Appl. Meteorol. Clim.*, 10 53, 1636–1658, doi:10.1175/JAMC-D-13-0312.1, 2014. 18068, 18080
- Lance, S., Brock, C. A., Rogers, D., and Gordon, J. A.: Water droplet calibration of the Cloud Droplet Probe (CDP) and in-flight performance in liquid, ice and mixed-phase clouds during ARCPAC, *Atmos. Meas. Tech.*, 3, 1683–1706, doi:10.5194/amt-3-1683-2010, 2010. 18071
- 15 Lawson, R. P., O'Connor, D., Zmarzly, P., Weaver, K., Baker, B., Mo, Q., and Jons-son, H.: The 2D-S (Stereo) probe: design and preliminary tests of a new airborne, high-speed, high-resolution particle Imaging probe, *J. Atmos. Ocean. Tech.*, 23, 1462–1477, doi:10.1175/JTECH1927.1, 2006. 18071
- Lloyd, G., Choularton, T. W., Bower, K. N., Gallagher, M. W., Flynn, M., Farrington, R., Crosier, J., and Connolly, P. J.: The Origins of Ice Crystals Measured in Mixed Phase Clouds at High-Alpine Site Jungfraujoch, *Atmos. Chem. Phys. Discuss.*, in press, 2015. 18068, 20 18079, 18084
- Magono, C. and Lee, C. W.: Meteorological classification of natural snow crystals, *J. Fac. Sci., Hokkaido Univ., Series VII*, 2, 321–335, 1966. 18067
- Mitchell, D. L., Zhang, R., and Pitter, R. L.: Mass-dimensional relationships for ice particles and the influence of riming on snowfall rates, *J. Appl. Meteorol.*, 29, 153–163, doi:10.1175/1520-0450(1990)029<0153:MDRFIP>2.0.CO;2, 1990. 18067, 18072, 18095
- 25 Mosimann, L., Weingartner, E., and Waldvogel, A.: An analysis of accreted drop sizes and mass on rimed snow crystals, *J. Atmos. Sci.*, 51, 1548–1558, doi:10.1175/1520-0469(1994)051<1548:AAOADS>2.0.CO;2, 1994. 18072
- 30 Ono, A.: The shape and riming properties of ice crystals in natural clouds, *J. Atmos. Sci.*, 26, 138–147, doi:10.1175/1520-0469(1969)026<0138:TSARPO>2.0.CO;2, 1969. 18067
- Panziera, L. and Hoskins, B.: Large snowfall events in the south-eastern Alps, *Weather*, 63, 88–93, doi:10.1002/wea.178, 2008. 18082

**Riming in winter  
alpine snowfall  
during CLACE 2014**

J. Grazioli et al.

Title Page

Abstract

Introduction

Conclusions

References

Tables

Figures



Back

Close

Full Screen / Esc

Printer-friendly Version

Interactive Discussion



- Pinsky, M. B. and Khain, A. P.: Some effects of cloud turbulence on water-ice and ice-ice collisions, *Atmos. Res.*, 48, 69–86, 1998. 18067, 18076
- Pruppacher, H. R. and Klett, R. L.: *Microphysics of Clouds and Precipitation*, 2nd edn., no. 18 in *Atmospheric and Oceanographic Sciences Library*, Kluwer Academic Press, doi:10.1080/02786829808965531, 1997. 18066
- Rangno, A. L.: Fragmentation of freezing drops in shallow maritime frontal clouds, *J. Atmos. Sci.*, 65, 1455–1466, doi:10.1175/2007JAS2295.1, 2008. 18068
- Rauber, R. M. and Tokay, A.: An explanation for the existence of supercooled water at the top of cold clouds, *J. Atmos. Sci.*, 48, 1005–1023, doi:10.1175/1520-0469(1991)048<1005:AEFTEO>2.0.CO;2, 1991. 18067, 18076
- Ryzhkov, A. V., Giangrande, S. E., Melnikov, V. M., and Schuur, T. J.: Calibration issues of dual-polarization radar measurements, *J. Atmos. Ocean. Tech.*, 22, 1138–1155, doi:10.1175/JTECH1772.1, 2005. 18100
- Schneebeli, M., Dawes, N., Lehning, M., and Berne, A.: High-resolution vertical profiles of polarimetric X-band weather radar observables during snowfall in the Swiss Alps, *J. Appl. Meteorol. Clim.*, 52, 378–394, doi:10.1175/JAMC-D-12-015.1, 2013. 18068, 18070, 18073
- Scipion, D., Mott, R., Lehning, M., Schneebeli, M., and Berne, A.: Seasonal small-scale spatial variability in alpine snowfall and snow accumulation, *Water Resour. Res.*, 49, 1446–1457, doi:10.1002/wrcr.20135, 2013. 18070
- Straka, J. M. and Mansell, E. R.: A bulk microphysics parameterization with multiple ice precipitation categories, *J. Appl. Meteorol.*, 44, 445–466, doi:10.1175/JAM2211.1, 2005. 18066
- Straka, J. M., Zrnich, D. S., and Ryzhkov, A. V.: Bulk hydrometeor classification and quantification using polarimetric radar data: synthesis of relations, *J. Appl. Meteorol.*, 39, 1341–1372, 2000. 18068
- Takahashi, T.: Influence of liquid water content and temperature on the form and growth of branched planar snow crystals in a cloud, *J. Atmos. Sci.*, 71, 4127–4142, doi:10.1175/JAS-D-14-0043.1, 2014. 18067, 18078
- Torlaschi, E. and Gingras, Y.: Standard deviation of the copolar correlation coefficient for simultaneous transmission and reception of vertical and horizontal polarized weather radar signals, *J. Atmos. Ocean. Tech.*, 20, 760–766, doi:10.1175/1520-0426(2003)20<760:SDOTCC>2.0.CO;2, 2003. 18077
- Vardiman, L.: The generation of secondary ice particles in clouds by crystal-crystal collision, *J. Atmos. Sci.*, 35, 2168–2180, 1978. 18068, 18079, 18084

Westbrook, C. D. and Illingworth, A. J.: Evidence that ice forms primarily in super-cooled liquid clouds at temperatures  $> -27^{\circ}\text{C}$ , *Geophys. Res. Lett.*, 38, L14808, doi:10.1029/2011GL048021, 2011. 18078

5 Yano, J.-I. and Phillips, V. T. J.: Ice-ice collisions: an ice multiplication process in atmospheric clouds, *J. Atmos. Sci.*, 68, 322–333, doi:10.1175/2010JAS3607.1, 2011. 18068, 18079, 18084

10 Zieger, P., Kienast-Sjögren, E., Starace, M., von Bismarck, J., Bukowiecki, N., Baltensperger, U., Wienhold, F. G., Peter, T., Ruhtz, T., Collaud Coen, M., Vuilleumier, L., Maier, O., Emili, E., Popp, C., and Weingartner, E.: Spatial variation of aerosol optical properties around the high-alpine site Jungfrauoch (3580 m.a.s.l.), *Atmos. Chem. Phys.*, 12, 7231–7249, doi:10.5194/acp-12-7231-2012, 2012. 18069

**Riming in winter  
alpine snowfall  
during CLACE 2014**

J. Grazioli et al.

Title Page

Abstract

Introduction

Conclusions

References

Tables

Figures



Back

Close

Full Screen / Esc

Printer-friendly Version

Interactive Discussion





## Riming in winter alpine snowfall during CLACE 2014

J. Grazioli et al.

**Table 2.** List of the 6 rimed phases, subset of the events of 1, during which rimed precipitation was dominant according to the radar-based GTB2015 classifier.

Label	Start (UTC) MM-DD HH:mm	Duration [h]
EV3	02-01 17:00	9
EV4	02-04 00:00	3
EV5	02-05 18:00	2
EV6	02-07 08:30	2
EV7	02-08 20:00	1.5
EV13	02-22 19:30	2.5

[Title Page](#)[Abstract](#)[Introduction](#)[Conclusions](#)[References](#)[Tables](#)[Figures](#)[Back](#)[Close](#)[Full Screen / Esc](#)[Printer-friendly Version](#)[Interactive Discussion](#)

Riming in winter  
alpine snowfall  
during CLACE 2014

J. Grazioli et al.

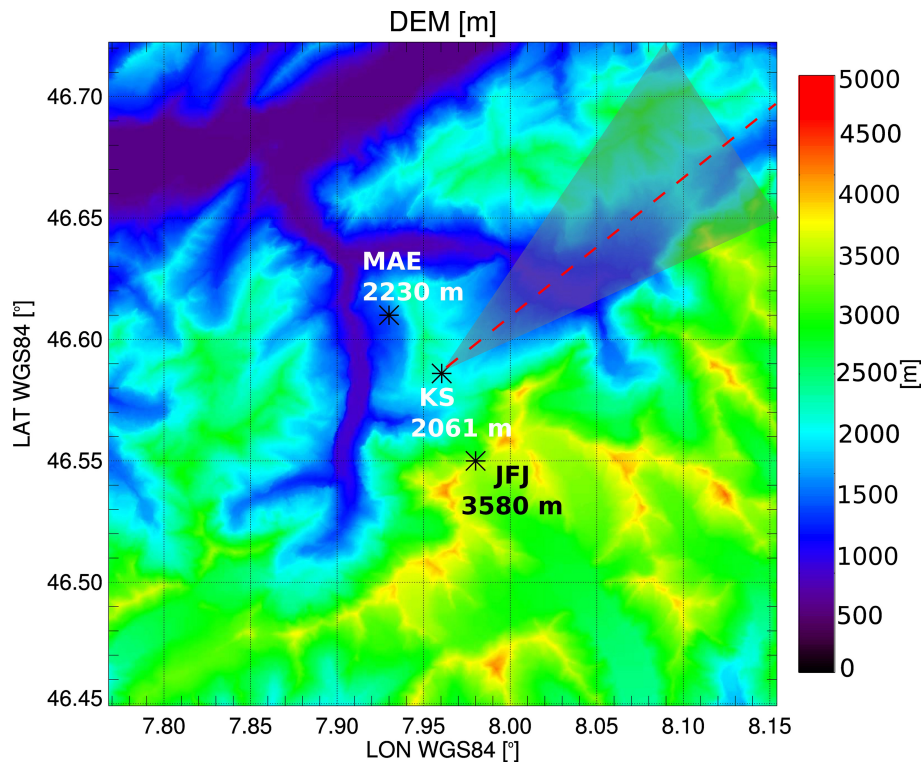


**Figure 1.** Location of the main measurement sites of CLACE 2014 that are considered here. The locations are highlighted on a digital elevation model of the area. The gray shade highlights the area of the domain covered by radar PPIs while the red line indicates the direction of the RHI employed in the analysis of the manuscript.

[Title Page](#)[Abstract](#)[Introduction](#)[Conclusions](#)[References](#)[Tables](#)[Figures](#)[◀](#)[▶](#)[◀](#)[▶](#)[Back](#)[Close](#)[Full Screen / Esc](#)[Printer-friendly Version](#)[Interactive Discussion](#)

Riming in winter  
alpine snowfall  
during CLACE 2014

J. Grazioli et al.

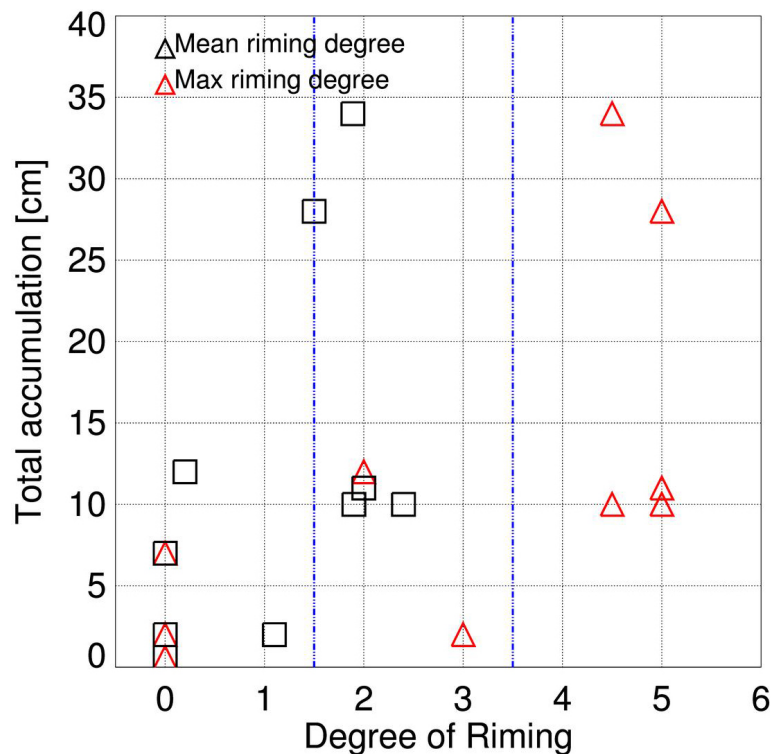


**Figure 2.** Relation between average (or maximum) degree of riming and snowfall accumulation measured during 12 precipitation events occurring at Stony Brook, New York (USA). The values displayed here correspond to tabulated values available in Colle et al. (2014). The blue vertical lines separate lightly, moderately, and heavily rimed particles according to Mitchell et al. (1990).

[Title Page](#)[Abstract](#)[Introduction](#)[Conclusions](#)[References](#)[Tables](#)[Figures](#)[◀](#)[▶](#)[◀](#)[▶](#)[Back](#)[Close](#)[Full Screen / Esc](#)[Printer-friendly Version](#)[Interactive Discussion](#)

## Riming in winter alpine snowfall during CLACE 2014

J. Grazioli et al.

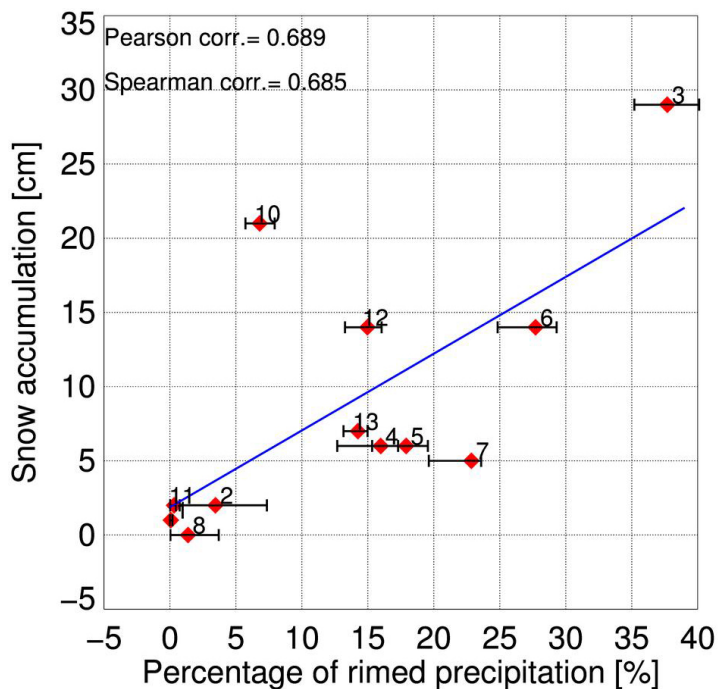


**Figure 3.** Relation between the percentage of rimed precipitation (PRP, retrieved by means of radar data) and snowfall accumulation, for the events listed in Table 1. The error bars represent the 5 and 95 % quantiles of PRP values calculated for maximum altitudes  $z_2$  (in Eq. 1) varying between 2250 and 4000 m. A linear regression line (in blue) is used to illustrate the average trend.

Title Page

Abstract

Introduction

Conclusions

References

Tables

Figures

◀

▶

◀

▶

Back

Close

Full Screen / Esc

Printer-friendly Version

Interactive Discussion



## Riming in winter alpine snowfall during CLACE 2014

J. Grazioli et al.

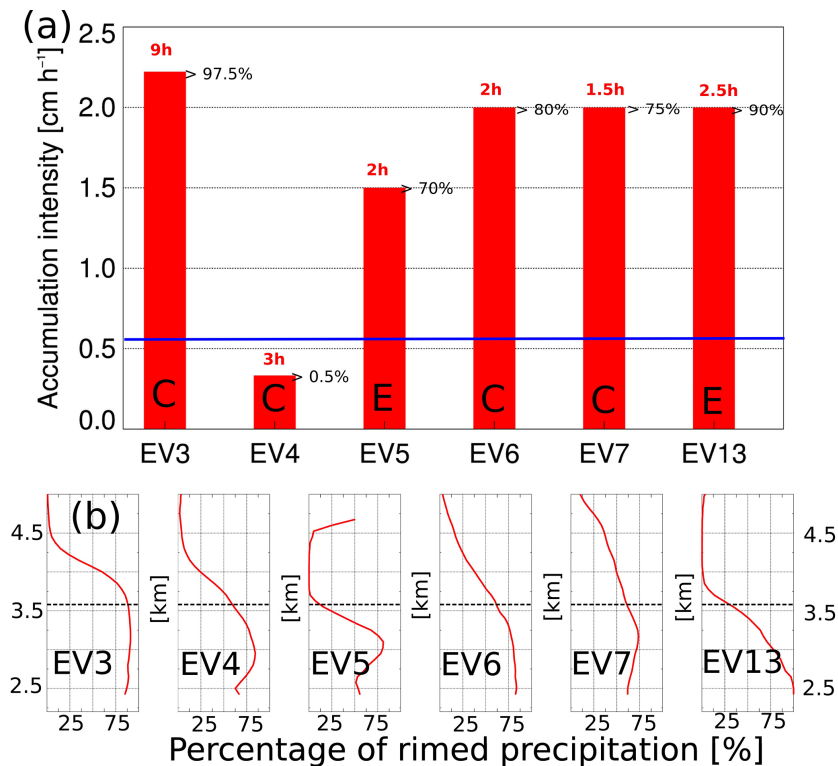


**Figure 4.** Summary characteristics of the 6 cases where riming is identified as dominant mechanism (as listed in Table 2). **(a)** Mean snowfall accumulation rate measured at MAE. The red number on top of each bar indicates the duration of the rimed time step. The number on the right side of the bars are the closest quantiles of the distribution of all snowfall events of the same duration in the same location (data from 2000 to 2014). The letters C and E refer to cases indicated in the text as “Core” and “Edge”, respectively. The blue line indicates the mean value (during precipitation only) of CLACE 2014. **(b)** Average vertical profile of the percentage of rimed precipitation PRP [%] during the selected timesteps.

## Riming in winter alpine snowfall during CLACE 2014

J. Grazioli et al.

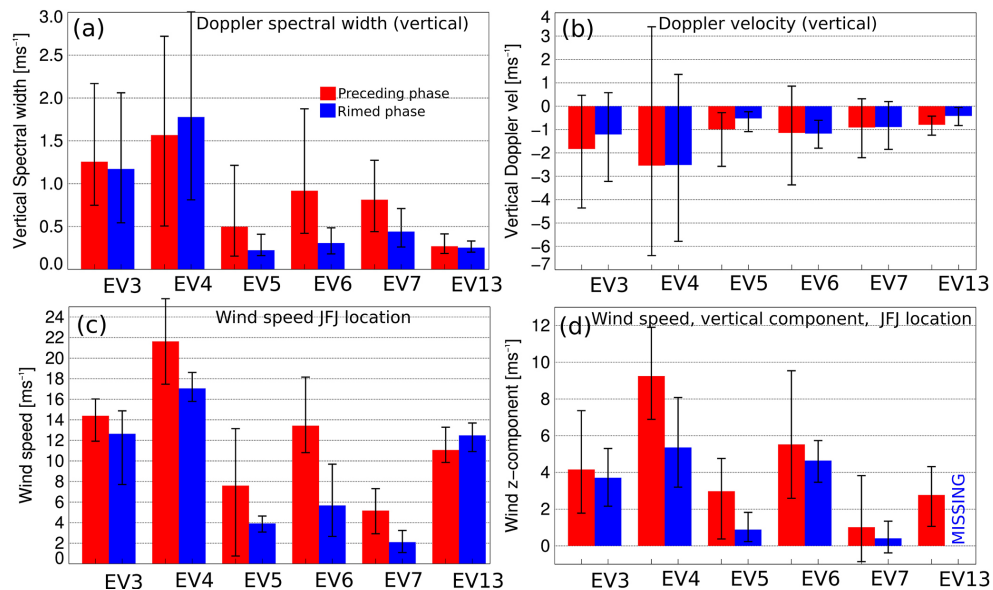


**Figure 5.** Measurements of wind, turbulence, and fall velocities before (red histograms) and during (blue histograms) the 6 “rimed phases” shown in Fig. 4. Panels (a, b) show radar data (only for altitude around the JFJ location:  $3580 \pm 100$  m), while panels (c, d) show data collected at the JFJ location. (a) Doppler spectral width [ $\text{m s}^{-1}$ ] from radar vertical profiles (i.e. at vertical incidence). (b) Doppler velocity [ $\text{m s}^{-1}$ ] from radar vertical profiles. (c) Wind speed (data from MeteoSwiss station) [ $\text{m s}^{-1}$ ]. (d) Vertical component of the wind (sonic anemometer data) [ $\text{m s}^{-1}$ ].

[Title Page](#)
[Abstract](#)
[Introduction](#)
[Conclusions](#)
[References](#)
[Tables](#)
[Figures](#)

[Back](#)
[Close](#)
[Full Screen / Esc](#)
[Printer-friendly Version](#)
[Interactive Discussion](#)


## Riming in winter alpine snowfall during CLACE 2014

J. Grazioli et al.

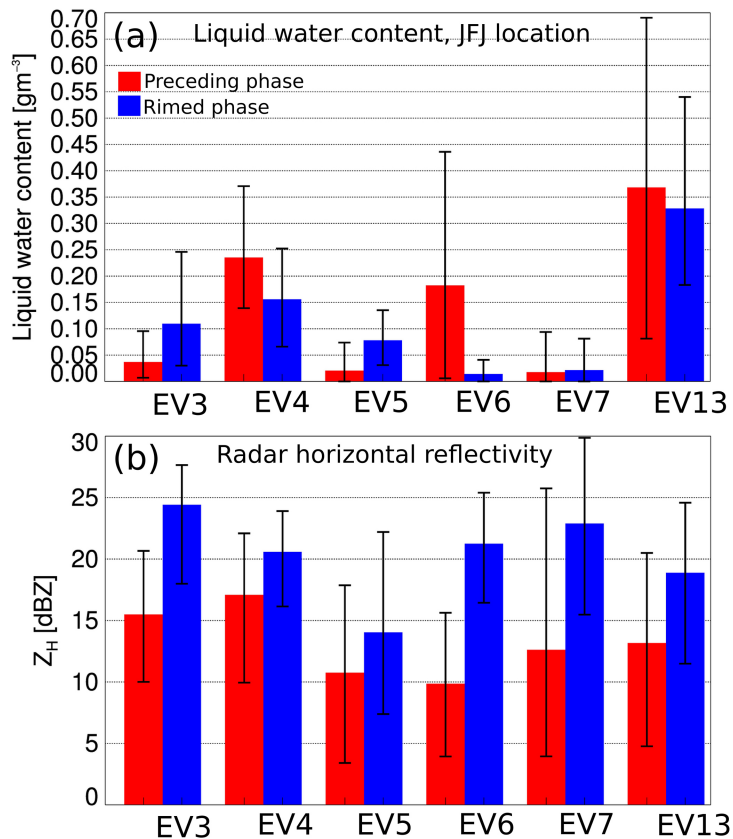


**Figure 6.** As in Fig. 5 for  $Z_H$  and LWC. **(a)** Liquid water content LWC [ $\text{gm}^{-3}$ ] measured at the JFJ location. **(b)** Radar horizontal reflectivity factor  $Z_H$  [dBZ] from altitudes around the JFJ location:  $3580 \pm 100$  m.

## Riming in winter alpine snowfall during CLACE 2014

J. Grazioli et al.

Title Page

Abstract

Introduction

Conclusions

References

Tables

Figures



Back

Close

Full Screen / Esc

Printer-friendly Version

Interactive Discussion

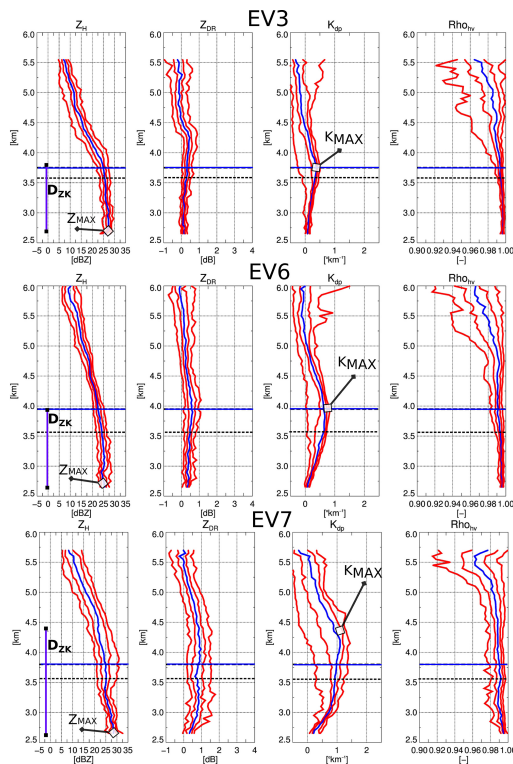


**Figure 7.** Vertical structure of polarimetric radar observations extracted from a single RHI of each selected cases. The blue horizontal line indicates the estimated altitude of the  $-15^{\circ}\text{C}$  temperature level while the dashed black line indicates the altitude of JFJ. The polarimetric variables are extracted considering a maximum elevation angle of  $45^{\circ}$  (the effect of incidence is corrected with the method of Ryzhkov et al., 2005). The red curves indicate quantiles at 5, 25, 75 and 95 % while the blue curve indicates the median. EV3 shows RHI data collected on 01 February 2014, 23:00 UTC. EV6 shows data collected on 07 February 2014, 10:05 UTC. EV7 shows data collected on 08 February 2014, 21:00 UTC.

Riming in winter  
alpine snowfall  
during CLACE 2014

J. Grazioli et al.

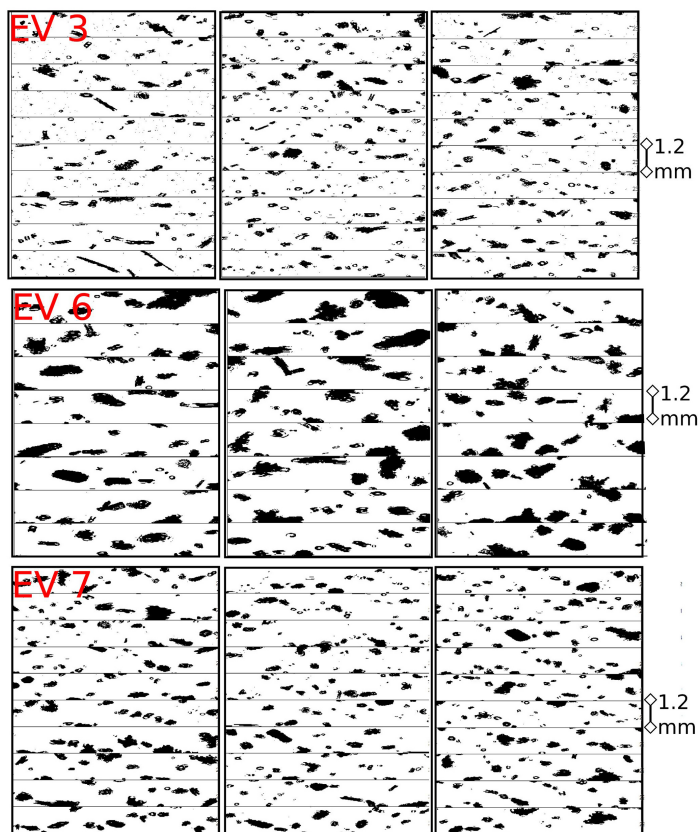


**Figure 8.** Particle images collected at the JFJ location by a 2D-S particle imager. Three cases are shown, corresponding to the polarimetric observations of Fig. 7. Top panel: EV3, on 01 February 2014, around 23:00 UTC. Mid panel: EV6 on 6 February 2014, around 10:00 UTC. Bottom panel: EV7 on 08 February 2014, around 21:00 UTC.

[Title Page](#)[Abstract](#)[Introduction](#)[Conclusions](#)[References](#)[Tables](#)[Figures](#)[◀](#)[▶](#)[◀](#)[▶](#)[Back](#)[Close](#)[Full Screen / Esc](#)[Printer-friendly Version](#)[Interactive Discussion](#)

Riming in winter  
alpine snowfall  
during CLACE 2014

J. Grazioli et al.

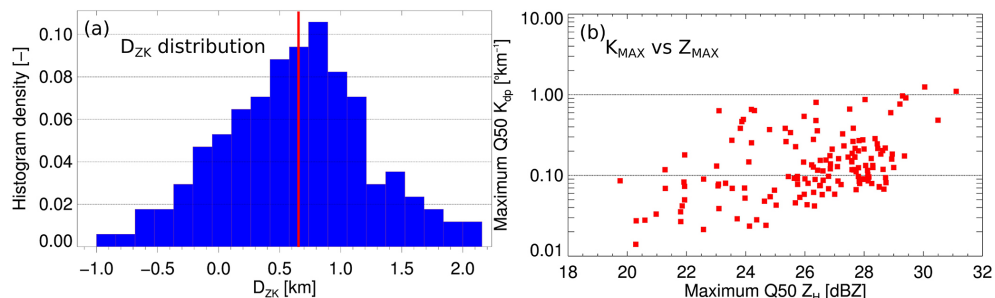


**Figure 9.** (a) Frequency distribution (i.e. sample histogram) of  $D_{zk}$  [km] values. (b) Scatterplot of  $K_{MAX}$  [° km<sup>-1</sup>] vs.  $Z_{MAX}$  [dBZ]. The graphs are calculated for all the time intervals listed in Table 2, and the quantities displayed are shown in Fig. 7.

Riming in winter  
alpine snowfall  
during CLACE 2014

J. Grazioli et al.

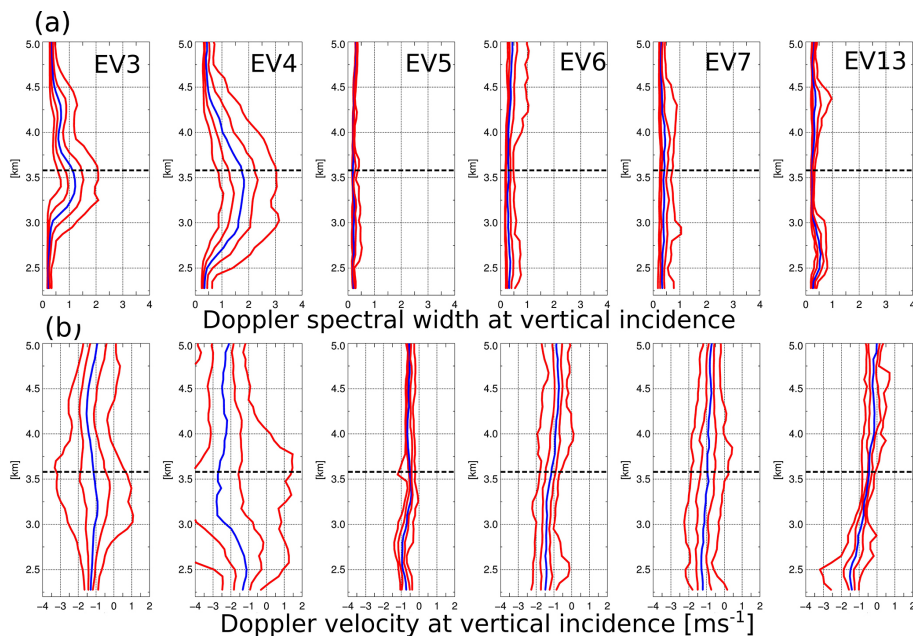


**Figure 10.** Vertical structure of: **(a)** Doppler velocity, and **(b)** Doppler spectral width over the whole duration of EV3, EV4, EV5, EV6, EV7, EV13. Both variables are measured at vertical incidence angles.

[Title Page](#)[Abstract](#)[Introduction](#)[Conclusions](#)[References](#)[Tables](#)[Figures](#)[Back](#)[Close](#)[Full Screen / Esc](#)[Printer-friendly Version](#)[Interactive Discussion](#)

Riming in winter  
alpine snowfall  
during CLACE 2014

J. Grazioli et al.

Title Page

Abstract

Introduction

Conclusions

References

Tables

Figures



Back

Close

Full Screen / Esc

Printer-friendly Version

Interactive Discussion

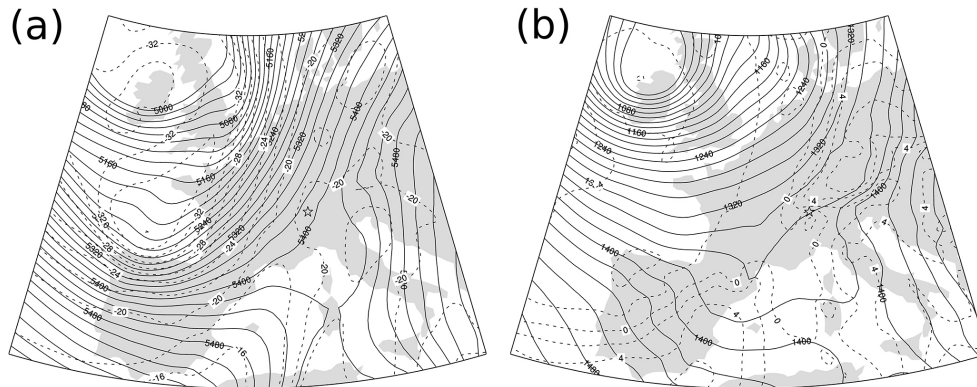


**Figure 11.** (a) 500 hPa and (b) 850 hPa geopotential height [m] (continuous lines) and temperature [°C] (dashed lines) over Central Europe at 12:00 UTC on the 02 February 2014. The geographical location of the CLACE campaign is indicated by a star. The atmospheric fields are derived by ERA-Interim reanalysis grids at  $0.5^\circ \times 0.5^\circ$  horizontal resolution.

Riming in winter  
alpine snowfall  
during CLACE 2014

J. Grazioli et al.

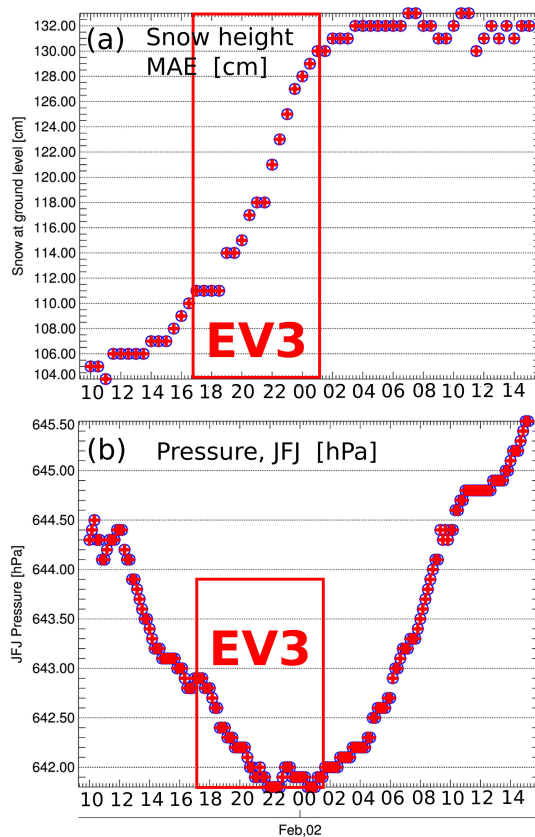


**Figure 12.** Evolution of: **(a)** snow accumulation at the ground level [cm], measured at the MAE site, **(b)** in-situ environmental pressure [hPa] measured at the JFJ location during EV3.



Riming in winter  
alpine snowfall  
during CLACE 2014

J. Grazioli et al.

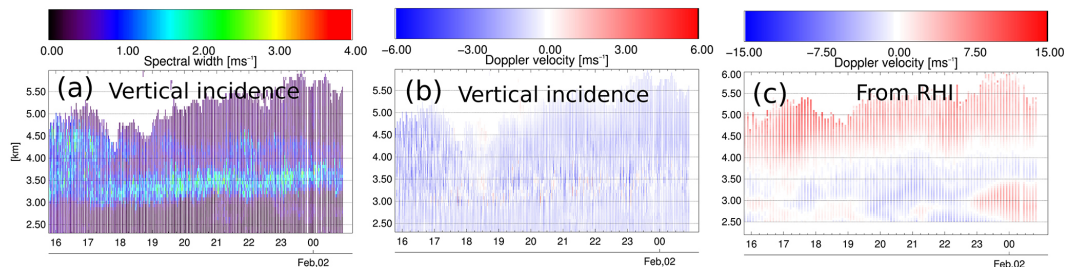


**Figure 13.** Time evolution of the vertical structure of Doppler-related variables during EV3. **(a)** Doppler spectral width at vertical incidence [ $\text{m s}^{-1}$ ]. **(b)** Doppler velocity at vertical incidence [ $\text{m s}^{-1}$ ]. **(c)** Doppler velocity from RHI scans [ $\text{m s}^{-1}$ ]. Each observation of panel **(c)** is the mean over the same height of all the observations collected during an RHI scan. Only one RHI direction ( $\approx 45^\circ$  North to East) is used to generate such a plot.

[Title Page](#)[Abstract](#)[Introduction](#)[Conclusions](#)[References](#)[Tables](#)[Figures](#)[◀](#)[▶](#)[◀](#)[▶](#)[Back](#)[Close](#)[Full Screen / Esc](#)[Printer-friendly Version](#)[Interactive Discussion](#)



## Riming in winter alpine snowfall during CLACE 2014

J. Grazioli et al.

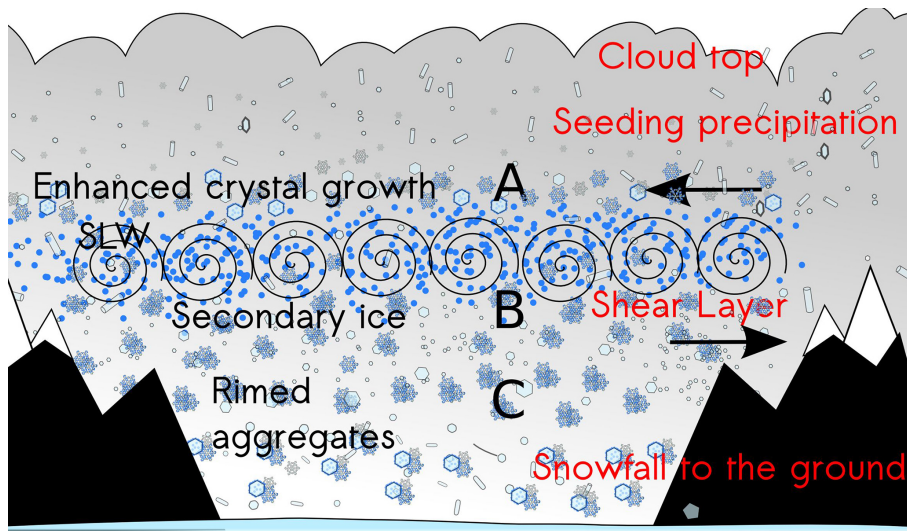


**Figure 15.** Schematic representation of the role of turbulence observed during EV3. The label “A” indicates area of enhanced  $Z_{DR}$ , label “B” enhanced  $K_{dp}$ , and label “C” enhanced  $Z_H$ .

Title Page

Abstract

Introduction

Conclusions

References

Tables

Figures



Back

Close

Full Screen / Esc

Printer-friendly Version

Interactive Discussion

